

Emergent properties of collective gene expression patterns in multicellular systems

Matthew Smart^{1,*} and Anton Zilman^{1,2,*}

¹ *Department of Physics, University of Toronto, 60 St George St, Toronto, ON M5S 1A7, Canada*

² *Institute for Biomedical Engineering, University of Toronto, 164 College St, Toronto, ON M5S 3G9, Canada*

*Correspondence: msmart@physics.utoronto.ca, zilmana@physics.utoronto.ca

Multicellular organisms are composed of a wide range of stable tissues containing different cell types. It remains unclear how a large number of interacting cells can precisely coordinate their gene expression during tissue self-organization. Here we develop a spin glass model of tissue gene expression which accounts for intracellular and intercellular gene regulation. The model provides a theoretical framework for tissue self-organization, with stable tissue configurations corresponding to local minima of the gene expression landscape. Intracellular gene regulation is defined using a Hopfield network, which enforces the stability of certain cell types in the absence of signaling. We represent multicellular tissue by a graph of interacting Hopfield networks. The edges of this graph represent cell-cell signaling which regulates the gene expression of adjacent cells. By tuning the signaling strength, the model exhibits a cascade of transitions between different self-organized tissue states. We specifically consider random cell-cell signaling networks and show that several properties of the distribution of stable tissues are preserved for different realizations. Counterintuitively, we find that random signaling networks tend to stabilize highly ordered tissue states. These results may explain why collections of cells in distinct organisms robustly self-organize into relatively simple tissues even when the microscopic interactions which drive the system are highly disordered.

1. INTRODUCTION

Multicellular organisms are composed of a wide range of self-organized tissues that are distinguished by the spatial arrangement of cell types they contain. The tissue self-organization process, which results in many cells collectively exhibiting a spatial pattern of gene expression, is a fundamental and mysterious requirement of multicellular life. It remains unclear how very large numbers of interacting cells are able to precisely coordinate their gene expression during development, homeostasis, and in response to infection. A key turning point was the discovery that cells can be experimentally “reprogrammed” to an undifferentiated state by turning specific genes on or off (1). This revolutionized our understanding of gene regulation within single cells and tissue. It is now widely recognized that cellular phenotypes are highly plastic and may be modified not only *in vitro* (1, 2) but also *in vivo*. Such cell type transitions are critical for proper tissue homeostasis and wound healing (3–6), leading to a very dynamic picture of tissue self-organization. Accordingly, disruption of the self-organized tissue state through gene regulatory perturbations is implicated in the pathogenesis of many diseases, most notably cancer (7–10).

A major challenge for understanding tissue self-organization is the complexity of gene regulation. Despite this complexity, many biological processes are strikingly precise. Motivated by the regularity of cell fate specification during development, Waddington presciently put forward the concept of an “epigenetic landscape” in the 1950s (11). This seminal concept has been mathematically expanded as a result of experimental advances (12–15). In particular, modern experimental techniques such as single-cell RNA sequencing (scRNA-seq) have generated enormous amounts of transcriptomic data (16–18). Clusters in the data represent stable regions in single-cell gene expression space, and can

therefore be thought of as dynamical attractors – the valleys of the epigenetic landscape. The large number of observed clusters in mammalian scRNA-seq data indicates that the dynamical system governing single-cell state is nonlinear and high-dimensional. This must be accounted for to accurately describe tissue gene expression.

While cell state is regulated by intracellular mechanisms, it is also tightly regulated by extrinsic factors that mediate interactions between different cells. Yet there is a lack of models which can describe the gene regulation at the single-cell and tissue levels. Classical work which focused on the tissue level demonstrated that spatiotemporal patterns can be generated from just two diffusing morphogens (19). However, this work and modern variants use partial differential equations to describe a “continuum” of cells. They are not appropriate to describe single-cell gene regulatory effects, for instance, cellular autonomy in the absence of morphogens. Several recent works have partially addressed this concern, using cellular automata to integrate single-cell and tissue level effects (20–22). Computational approaches which additionally consider physical interactions such as adhesion have recently been reviewed (23). Overall, previous works have focused on analytically studying the case of just one or two interacting genes, or use large, highly tuned simulations to study specific experimental systems.

Significant international effort is underway through the Human Cell Atlas (HCA) project (16, 18) to catalog the cells found in human tissue from development to adulthood and in disease. The large volume of scRNA-seq data, which can measure gene expression in millions of single cells at a time, allow us to observe cell state in unprecedented detail. This has enabled reconsideration of classical cell type categorizations such as “macrophage” or “fibroblast”. A data-driven view is that cell types should be defined based on clusters in the transcriptomic data, as the expression

signatures of observed clusters tend to align with known sets of marker genes expressed by *in vivo* cell types (17, 18, 24). However, an integrated model of how gene regulation proceeds at the intra- and intercellular levels is necessary to fully interpret the associated data. This will ultimately address fundamental questions such as whether cell types are discrete or continuous entities, as well as related experimental questions (e.g. organoid growth and differentiation protocols (25)).

The high-dimensionality of gene regulatory networks remains a significant challenge for modeling tissue self-organization. As a representative example, mammalian cells have on the order of 10^4 protein-coding genes, with $\sim 10^3$ identified as transcription factors – genes that regulate the expression of other genes (26). Due to the limited degree to which gene-gene interactions are quantitatively characterized in various organisms, physically parameterized models of gene networks are of limited utility. Additionally, the stability of certain gene expression signatures in the scRNA-seq data is an experimental constraint that needs to be accounted for. Thus we focus on minimal models which can encode a set of high-dimensional gene expression patterns as dynamical attractors. We specifically employ Hopfield Networks (HNs) (27, 28) which have been used to describe reprogramming in individual cells (29, 30).

In the next section, we present a model of multicellular gene expression which unifies the single-cell and tissue levels of biological organization by coupling the transcriptomic states of interacting cells in a systematic, tunable manner. In the Results section, we demonstrate how different choices of cell-cell interactions can cause the multicellular system to self-organize into a broad range of collective spatial patterns. To examine how cell-cell interactions control the development of such patterns, we consider an ensemble of tissues composed of non-interacting cells and tune the strength of signaling. This reveals a rich sequence of transitions in the space of tissue gene expression. In the strong signaling regime, we characterize the distribution of stable tissues and show that it may be partitioned into a relatively small number of tissue types. Our results suggest that several aspects of this distribution are invariant under different realizations of the random signaling rules. We conclude with a discussion of these results, which have implications for understanding the self-organization gene expression patterns in development and homeostasis. Our analysis may also inform our understanding of diseases that disrupt the phenotypic composition of tissues, such as autoimmunity and cancer.

2. MODEL

In this section we outline the model of multicellular gene expression. First, we introduce the fundamental unit of the model, the single cell. We then present the multicell model wherein single cells interact on a graph describing spatial coupling of cells. Finally, we explain how the cell-cell

interactions are incorporated. A concise overview of all terms and expressions in this section is given in SI Table 1.

2.1 Single-cell model

We assume that the phenotype of a single cell is defined by its gene expression pattern, where each gene is in a binary “on” or “off” state. This simplifying assumption follows Kauffman’s classical work (31). The state of the cell is then given by a binary vector $\mathbf{s} \in \{+1, -1\}^N$ where N is the number of genes and s_i denotes the state of gene i .

Stable single-cell phenotypes (cell types) are represented as attractors of the biological gene regulatory network (32). The transcriptome of a given cell type μ is denoted by ξ^μ (as an N -dimensional binary vector). Sequencing efforts have identified the stable transcriptomic signatures of a large set of p cell types $\{\xi^\mu\}_{\mu=1}^p$. The stability of each observed cell type ξ^μ is a key constraint for a candidate model of gene expression dynamics.

Hopfield networks (HN) (27, 28, 33) provide a tractable minimal model to encode such attractors. Mathematically, an HN is a form of Ising spin glass and is defined by the Hamiltonian (or “energy landscape”)

$$\mathcal{H}_0(\mathbf{s}) = -\frac{1}{2} \mathbf{s}^T \mathbf{J} \mathbf{s} - \mathbf{h}^T \mathbf{s}. \quad (1)$$

where \mathbf{h} is an applied field on each gene and the gene-gene interactions \mathbf{J} are chosen so that each pattern ξ^μ is a global minimum of Eq. (1) in the absence of an external field. Choosing \mathbf{J} based on a rule to encode a set of patterns as minima is commonly called pattern storage in the HN literature.

Because the gene expression vectors associated with cell types are typically correlated (i.e. non-orthogonal), we use the projection rule (34, 35) for pattern storage as in (29). Given an $N \times p$ matrix of cell type transcriptomes $\xi = [\xi^1 \ \xi^2 \ \dots \ \xi^p]$, the projection rule for storing the p patterns is

$$\mathbf{J}^{\text{proj}} = \xi (\xi^T \xi)^{-1} \xi^T, \quad (2)$$

which specifies an $N \times N$ matrix of gene-gene interactions. As in (34) we set the diagonal elements J_{ii} to zero.

Minima of the Hamiltonian Eq. (1) correspond to stable gene expression states. In the absence of noise or external signals \mathbf{h} , a given cell state $\mathbf{s} \in \{+1, -1\}^N$ will decrease its energy $\mathcal{H}_0(\mathbf{s})$ until it reaches a local minimum \mathbf{s}^* of \mathcal{H}_0 . The projection rule Eq. (2) ensures each cell type ξ^μ is a global minimum of \mathcal{H}_0 (34, 35).

This framework has been shown to recapitulate aspects of *in vitro* cellular reprogramming in single cells (29, 30). HNs have also been used in a variety of other biological contexts (36–40). To describe multicellular systems such as tissue, we next consider how cells may influence one another’s gene expression.

2.2 Multicellular model

To treat a multicellular system of M cells, we extend Eq. (1) by adding intercellular interaction terms. The

Hamiltonian for the collection of M cells, as a set of N -dimensional gene expression vectors $\{\mathbf{s}^a\}_{a=1}^M$, is

$$\mathcal{H}(\{\mathbf{s}^a\}) = \sum_a \mathcal{H}_0(\mathbf{s}^a) + \gamma \sum_a \sum_b A^{ab} f(\mathbf{s}^a, \mathbf{s}^b). \quad (3)$$

where the summation is over individual cells. The first sum describes the M individual cells, while the second sum contains the cell-cell couplings with a symmetric functional form $f(\mathbf{x}, \mathbf{y}) = f(\mathbf{y}, \mathbf{x})$. Biologically, these cell-cell interactions can be mediated by a variety of factors, and we detail a particular form for the coupling inspired by ligand-receptor signaling in Section 2.3. The spatial adjacency matrix \mathbf{A} defines which cells are interacting, with $A^{ab} = 1$ if a and b are neighbors (interact) and 0 otherwise. This graph representation of interacting cells is depicted in Fig. 1A.

The overall interaction strength is quantified by the global parameter $\gamma \geq 0$. As $\gamma \rightarrow 0$ the tissue acts as a collection of M independent, non-interacting cells. Beyond a certain threshold $\gamma > 0$ the system may exhibit emergent multicellular behavior, such as signaling dependent cell types or collective spatial patterns.

For simplicity, we assume an adjacency matrix corresponding to a square lattice. This choice is biologically inspired by cells interacting through paracrine signaling of secreted compounds over relatively short distances. While we focus on the two-dimensional case for ease of visualization, an arbitrary cell-cell interaction matrix can be chosen instead of the square lattice. Likewise, the interaction strength γ could also be distance-dependent instead of constant.

2.3 Cell-cell interactions

Many genes participate in cell-cell interactions by generating, sensing, or transducing signals that are sent between cells. For example, a cell may express and secrete signaling molecules (ligands) into the surrounding environment, which in turn affects the gene expression of neighboring cells that sense and respond to these signals. Each ligand may influence the expression of many genes in a target cell resulting in an intercellular gene-gene interaction network. We represent this network of sender-recipient signaling interactions via an $N \times N$ matrix \mathbf{W} , where W_{ij} represents the effect gene j (in a sender cell) has on gene i (in a recipient cell). A complete empirical \mathbf{W} is not yet available from the biological data and so we focus on the case of randomly sampled \mathbf{W} in Section 3.

The cell-cell signaling matrix \mathbf{W} effectively couples the gene regulatory networks of neighboring cells, and is depicted graphically in Fig. 1B. We denote the ‘‘signaling field’’ which cell b exerts on a neighboring cell a by $\mathbf{h}^{ab} = \gamma \mathbf{W} \mathbf{s}^b$, which acts as an applied field on the single-cell Hamiltonian for cell a , $\mathcal{H}_0(\mathbf{s}^a)$ (Eq. (1)). Summing over all neighbors gives the total applied field that the tissue collectively exerts on cell a ,

$$\mathbf{h}^a = \gamma \mathbf{W} \sum_b A^{ab} \mathbf{s}^b. \quad (4)$$

Note that this collective applied field is not static; it changes with the state of the tissue. This aspect is essential for the self-organizing properties of the model.

The collective applied field Eq. (4) we have chosen for our initial investigation depends only on the state of the sender cells. In principle, this function could also depend on the state of the recipient cell. For example, a cell which is not expressing certain receptors will not be able to sense and respond to the corresponding ligands. This more complex signaling form will be explored in future work.

When both \mathbf{J} and \mathbf{W} are symmetric, the collective behavior can be studied from a statistical mechanics perspective through the multicellular Hamiltonian introduced above. The choice of collective applied field in Eq. (4) corresponds to choosing $f(\mathbf{s}^a, \mathbf{s}^b) = -\frac{1}{2} \mathbf{s}^{aT} \mathbf{W} \mathbf{s}^b$ for the interaction terms in Eq. (3). The full multicellular Hamiltonian is then

$$\mathcal{H}(\{\mathbf{s}^a\}) = -\frac{1}{2} \sum_a \mathbf{s}^{aT} \mathbf{J} \mathbf{s}^a - \frac{\gamma}{2} \sum_a \sum_b A^{ab} \mathbf{s}^{aT} \mathbf{W} \mathbf{s}^b. \quad (5)$$

We also note that Eq. (5) can be compactly expressed as $\mathcal{H}(\mathbf{x}, \gamma) = -\frac{1}{2} \mathbf{x}^T \mathcal{J}(\gamma) \mathbf{x}$, where \mathbf{x} is an NM vector of each cell’s transcriptome concatenated, and the $NM \times NM$ interaction matrix $\mathcal{J}(\gamma)$ has a block form,

$$\mathcal{J}(\gamma) = \mathbf{I}_M \otimes \mathbf{J} + \mathbf{A} \otimes \gamma \mathbf{W}, \quad (6)$$

with \otimes denoting the Kronecker product for constructing block matrices and \mathbf{I}_M the $M \times M$ identity matrix. See Fig. 1C for an illustration of how $\mathcal{J}(\gamma)$ is constructed from its component matrices. The diagonal blocks correspond to the same intracellular gene interactions \mathbf{J} shared by all cells, whereas the off-diagonal blocks correspond to the intercellular signaling matrix \mathbf{W} tiled according to the adjacency matrix \mathbf{A} and scaled by γ .

Various types of block Ising models have been studied in different contexts (41–44), but they have largely been restricted to either two cells or to uniform off-diagonal interactions (i.e. constant W_{ij} or simple adjacency $A^{ab} = 1 - \delta^{ab}$). We are focused here on much more general off-diagonal interactions (randomly sampled W_{ij} and structured adjacency matrices; see Section 3). Of note, Refs. (45–47) studied disordered ‘‘multi-species’’ block systems with an arbitrary number of cells, but they consider alternative couplings between cells and do not focus on the deterministic limit.

Although in this work we consider discrete gene expression states, we note that related continuous state models known as coupled map lattices (48) have been used to describe lattices of interacting cells (49–51). These works focused on a few genes or underlying cell types, whereas the approach we outline is inherently scalable to many genes and cell types.

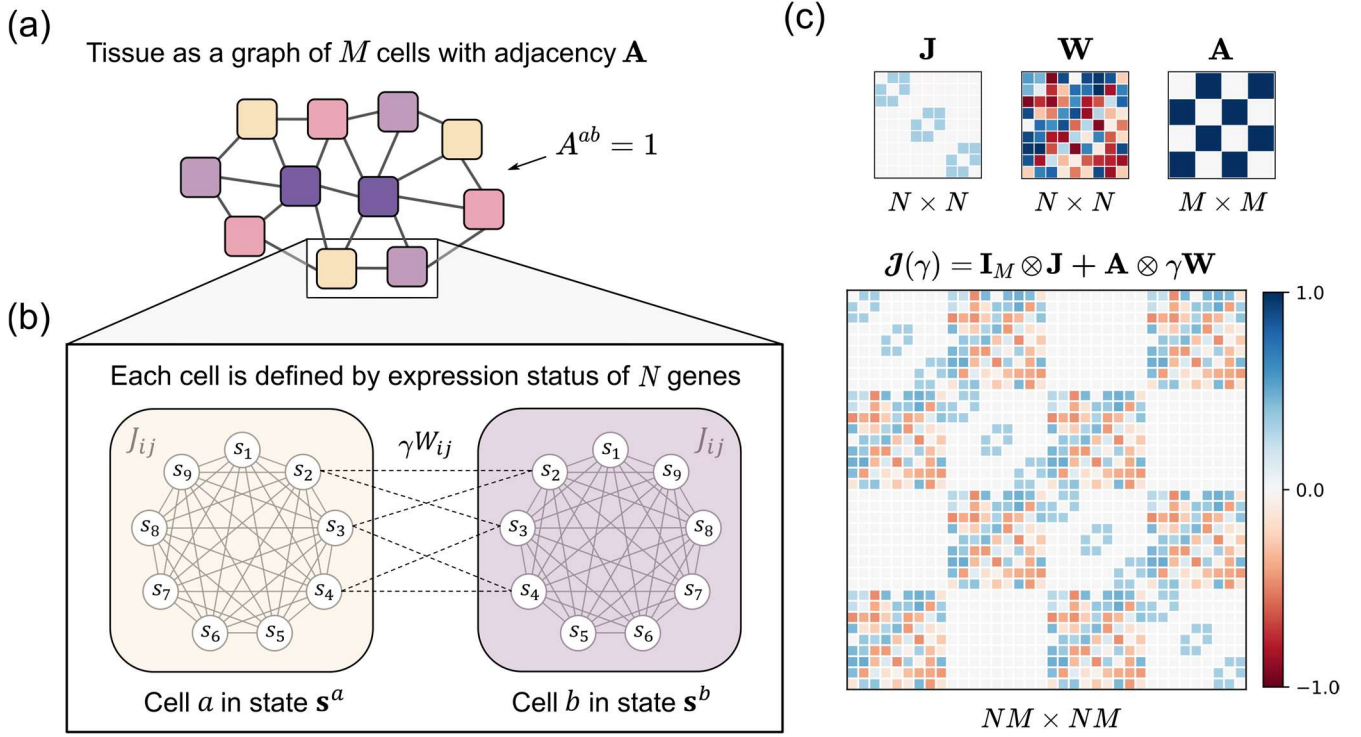


Fig. 1. Multicellular model. (A) Biological tissue consisting of M interacting cells is represented by a graph. Cells are depicted as squares with distinct colors denoting different gene expression states. Graph edges are defined by the adjacency matrix \mathbf{A} with $A^{ab} = 1$ if cells a, b interact, 0 otherwise. (B) Single cell state is defined by the expression status of N genes, $s_i \in \{+1, -1\}$, $i = 1, \dots, N$. We concisely denote the state of cell a by the N -dimensional vector \mathbf{s}^a . Every cell has the same intracellular gene regulatory rules specified by an $N \times N$ matrix J_{ij} . Adjacent cells interact according to a second $N \times N$ matrix W_{ij} which describes the effect that gene j in a “sender” cell has on gene i in a “recipient” cell. The cell-cell interaction strength γ tunes the magnitude of \mathbf{W} relative to \mathbf{J} . (C) The interaction matrix for tissue gene expression, denoted by $\mathcal{J}(\gamma)$, defines interactions between all NM genes in the multicellular system. To illustrate its construction, we show $\mathcal{J}(\gamma = 0.5)$ for particular choices of \mathbf{J} , \mathbf{W} , and \mathbf{A} (indicated above).

2.4 Gene expression dynamics

The minima of Eq. (5) correspond to stable configurations of the tissue (collective gene expression patterns). To identify them, we use a discrete analog of gradient descent on Eq. (5). However, our results are also relevant in the case of mild gene expression noise. We present the full stochastic update rule here for completeness, then introduce the deterministic limit.

We use Glauber dynamics (28, 52) as an asynchronous update rule for the single-cell spin glass Eq. (1) and its multicell extension Eq. (5). We emphasize that we are not focused on the dynamics itself, but rather in using it as a tool to sample the steady states which arise for interacting cells. For a given cell, the N genes are updated in a fixed sequential order (i.e. not in parallel) according to

$$p(s_i(t+1) \rightarrow 1) = \frac{1}{1 + \exp(-2\beta h_i^{\text{total}})} \quad (7)$$

where $h_i^{\text{total}} = \sum_j J_{ij} s_j(t) + h_i$, and β^{-1} represents the strength of the gene regulatory noise arising from various sources (analogous to thermal noise). The timestep t is

expressed in units of single gene updates. In the multicellular model, we update all cells (again in a fixed sequential update order) using Eq. (7). Note that the mean spin update is $\langle s_i(t+1) \rangle = \tanh(\beta h_i^{\text{total}})$.

In the deterministic limit ($\beta \rightarrow \infty$) of Eq. (7), the update rule for a single cell becomes $\mathbf{s}(t+N) = \text{sgn}(\mathbf{J}\mathbf{s}(t) + \mathbf{h})$, where $\text{sgn}(\cdot)$ is applied element-wise and the N genes are updated sequentially. A state is a fixed point of the update rule when $\mathbf{s} = \text{sgn}(\mathbf{J}\mathbf{s} + \mathbf{h})$. Note that the sequential update order does not impact whether a state is a fixed point. For $\mathbf{h} = \mathbf{0}$, it can be verified that the encoded cell types ξ^μ are fixed points when \mathbf{J} is defined via the projection rule of Eq. (2).

For the multicellular model, the deterministic update rule for each cell is

$$\mathbf{s}^a(t+N) = \text{sgn} \left(\mathbf{J}\mathbf{s}^a(t) + \gamma \mathbf{W} \sum_b A^{ab} \mathbf{s}^b(t) \right). \quad (8)$$

where $a \in \{1, \dots, M\}$. Tissue level updates can be expressed compactly using Eq. (6) as $\mathbf{x}(t+NM) = \text{sgn}(\mathcal{J}\mathbf{x}(t))$.

Very similar systems of equations have been used as continuous-time dynamical systems, most notably in Hopfield's classical work on associative memory (53). They take the form $\frac{du_i}{dt} = -\frac{u_i}{\tau_i} + \sum_j \tanh(\beta v_i)$ with $v_i \equiv \sum_j J_{ij} u_j + h_i$, $\tau_i > 0$. An analogous system has been applied to scRNA-seq data, where it generated experimentally validated predictions in the context of differentiation (24). Interestingly, this class of systems can also be used as "general-purpose" recurrent neural networks which may be trained to reproduce time series from other dynamical systems (54).

Finally, we note that the dynamics (Eqs. (7) and (8)) remain valid when either of \mathbf{J} , \mathbf{W} are asymmetric. In this case, the model becomes non-equilibrium and is known as an asymmetric kinetic Ising system (55–57). In addition to fixed

point attractors, non-equilibrium systems can exhibit oscillatory behavior which is necessary to describe phenomena such as the cell cycle or temporal spatial patterns. The non-equilibrium case will be investigated in future work.

3. RESULTS

To characterize the stable tissues which may self-organize in a given multicellular system, we collect deterministic fixed points from arbitrary initial conditions for a given choice of intracellular interactions \mathbf{J} , cell-cell interactions \mathbf{W} , and cell-cell adjacency matrix \mathbf{A} .

For simplicity and to facilitate visualization, we consider a low-dimensional system with $N = 9$ genes and $p = 3$ encoded single-cell types (shown in Fig. 2A). The set of cell

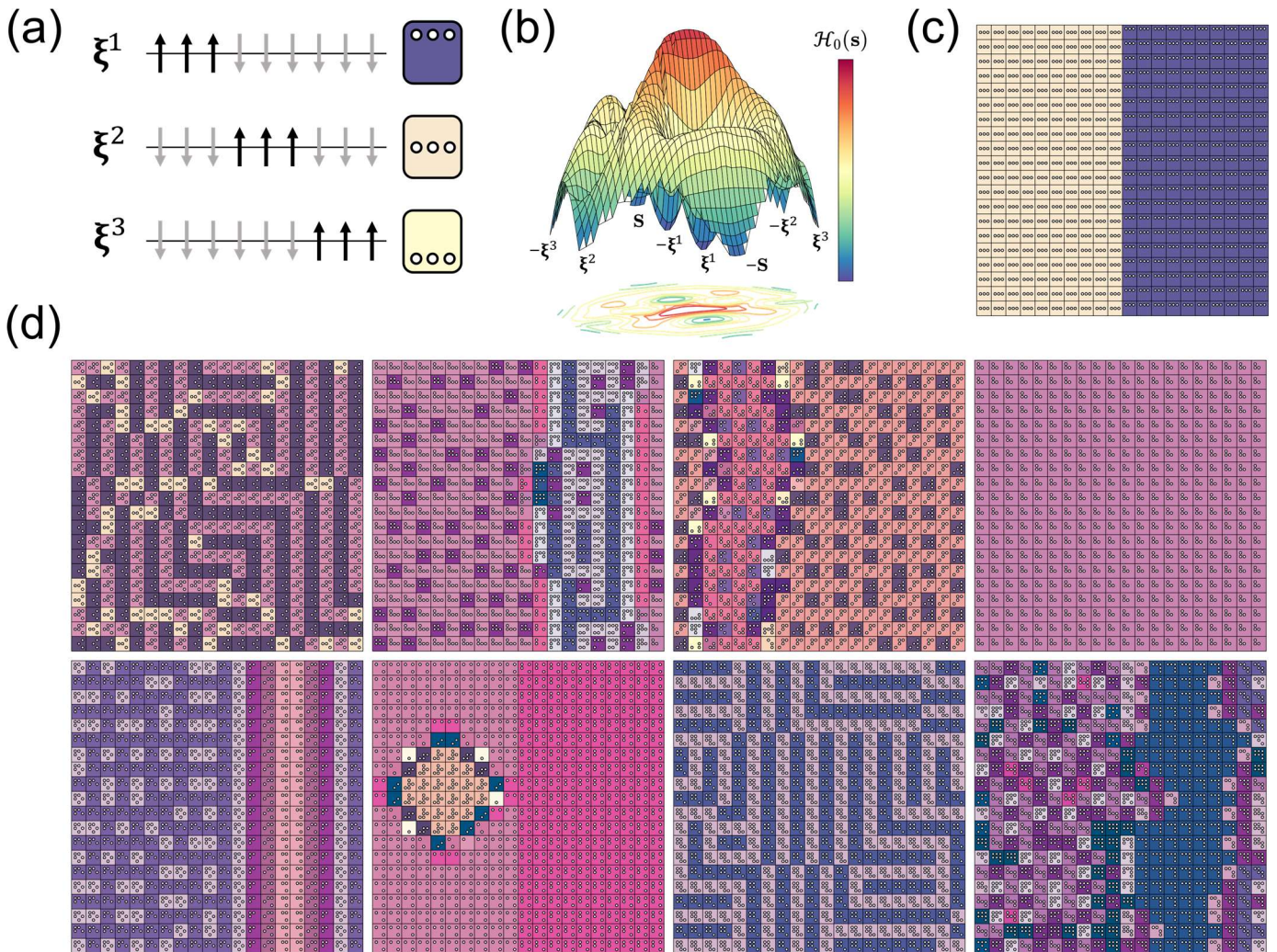


Fig. 2. Encoded cell types allow a variety of stable tissue patterns for varying signaling rules. (A) An example system with $N = 9$ genes and $p = 3$ single cell types $\{\xi^\mu\}_{\mu=1}^3$ defined by their gene expression patterns (arrow up/down denotes on/off). Each cell state is represented by a grid of up to N white dots where the presence (absence) of a dot indicates the associated gene is on (off). Additionally, each unique cell state $\mathbf{s} \in 2^N$ is assigned a unique color. The choice of patterns fixes the intracellular rules \mathbf{J} through the projection rule Eq. (2). (B) Two-dimensional embedding of the single cell energy landscape $\mathcal{H}_0(\mathbf{s})$ Eq. (1) (details in SI Text). (C) A 400 cell (20×20 grid) lattice initial condition is prepared with ξ^2 cells on the left half and ξ^1 cells on the right half. (D) Stable tissue patterns reached from the initial condition in C are found for eight random symmetric signaling rules $W_{ij} \sim U[-1,1]$ with $\gamma = 1$.

type gene expression vectors $\{\xi^\mu\}$ determines the intracellular gene regulatory interactions \mathbf{J} through the Hopfield projection rule Eq. (2) (Fig. 1C). The single-cell energy landscape Eq. (1) is depicted in Fig. 2B for the single-cell types from Fig. 2A (details in SI Text). In addition to the three encoded minima, there are five “spurious” minima consisting of the negation of each cell type, $-\xi^\mu$ (due to spin-flip symmetry of $\mathcal{H}(\mathbf{s})$), and the sum of the three types, $\pm\mathbf{S} = \pm\frac{1}{3}(\xi^1 + \xi^2 + \xi^3)$. Although some spurious minima may be biologically significant (29), others are likely not (e.g. the negations $-\xi^\mu$). We assume throughout this paper that $\mathbf{h} = \mathbf{0}$, but we note that certain minima can be eliminated using a global external field.

As mentioned previously, the cell-cell interaction matrix \mathbf{W} is not yet fully characterized experimentally. In addition to the many genes that have direct signaling roles (e.g. ligands and receptors), even more genes participate indirectly in signaling networks (e.g. as co-factors, downstream sensing molecules, activatable transcription factors, etc.) or as cargo for extracellular vesicles such as exosomes which can shuttle RNA between cells (58). In lieu of definitive data constraining \mathbf{W} (in contrast to the single-cell transcriptomics data constraining \mathbf{J}), we consider dense symmetric matrices, sampling the upper triangular elements as $W_{ij} \sim U[-1, 1]$ (see e.g. Fig. 1C).

3.1 Different signaling rules stabilize qualitatively distinct tissue types

We are first interested in assessing the range of possible tissues states which can self-organize under different cell-cell signaling rules. In particular, we fix all aspects of the model except for the cell-cell signaling matrix \mathbf{W} (i.e. we fix \mathbf{J} , \mathbf{A} , and γ). As mentioned above, \mathbf{J} is set by the choice of encoded single-cell types (Fig. 2A), and \mathbf{A} represents a square lattice. We then sample different realizations of $W_{ij} \sim U[-1, 1]$ and identify the tissues which self-organize starting from a fixed initial condition of the tissue gene expression.

In Fig. 2C we prepare an initial condition of $M = 400$ cells arranged on a 20×20 lattice. This choice mimics a 2D sheet of cells consisting of two different cell types: the left half is composed of cells in state ξ^2 and the right half is composed of cells in state ξ^1 (Fig. 2A depicts the single-cell types $\{\xi^\mu\}$ which are stable in the absence of signaling). This tissue state then evolves according to the regulatory rules, eventually reaching a local minimum of Eq. (5). The state of the tissue is visualized as follows: each square in the grid describes a cell at a particular location in space. The gene expression state of each given cell is visualized both quantitatively (through the presence/absence of $N = 9$ dots corresponding to “on” genes inside the square as in Fig. 2A) and qualitatively (each unique cell state $\mathbf{s} \in 2^N$ is assigned a unique color).

We identify fixed points reached from the initial condition in Fig. 2C for various interaction matrices \mathbf{W} sampled as described in Section 3.1, when the signaling strength γ is set

to 1. Several representative examples are displayed in Fig. 2D. Interestingly, sufficiently strong interactions can destabilize the encoded single-cell types $\{\xi^\mu\}$, and the set of stable tissue configurations reached by different choices of \mathbf{W} is quite diverse. Broadly speaking, the choice of \mathbf{W} typically stabilizes one of several “tissue types”. These tissue categories include homogeneous (all cells are in the same state), ordered layers, and maze-like (a few states which are spatially interwoven). More heterogeneous patterns are possible, as are multi-phasic patterns where different spatial regions of the tissue exhibit different patterns (such as homogeneous in one region and maze-like in another). The spatial features of the observed patterns also scale with the signaling range (Fig. S1).

Overall, different signaling rules \mathbf{W} can cause an arbitrary configuration of single-cells to self-organize into a variety of stable tissue configurations. These patterns are maintained through coherent signaling between the cells within their local neighborhoods (Eq. (4)). This tissue self-organization process is important for biological functions such as homeostasis in different organisms but is difficult to characterize experimentally due to the high-dimensionality of gene expression. This theoretical approach describes the formation and stabilization of collective gene expression patterns for particular choices of the gene regulatory parameters $(\mathbf{J}, \mathbf{W}, \gamma)$ and spatial organization of cells (\mathbf{A}) , which is useful for understanding how particular stable tissue states arise both *in vivo* and *in vitro*.

3.2 Tuning the signaling strength destabilizes single-cell types, leading to a rich sequence of tissue transitions

Complex organisms exhibit a broad range of stable tissue configurations. It remains unclear how such diversity arises in the context of genetically predefined intracellular and intercellular regulatory rules (i.e. \mathbf{J}, \mathbf{W} are fixed by the genome). In a given organism there are numerous “tissue types” that are distinguished by their cellular composition and spatial patterning. To carry out different functional roles, such tissue types are often strikingly distinct (e.g. adipose tissue and hepatic lobules). In addition to the macroscopic variation across tissue types, there can also be fine-scale variation in a given type. In this case, the tissues are constructed from the same set of unique cell states, but there is minor variation in cell number or spatial arrangement (e.g. the fingerprints of identical twins).

Here we characterize the diversity of stable tissue configurations in the multicellular model when the regulatory parameters \mathbf{J}, \mathbf{W} , and \mathbf{A} are fixed. We focus on how this diversity emerges as the cell-cell signaling strength γ is tuned, as might occur during development or as part of homeostasis and adaptation to environmental pressures.

As an illustrative example, in Fig. 3A we reconsider the initial condition from Fig. 2A and gradually increase γ for a particular choice of cell-cell signaling rules \mathbf{W} . Here we keep the same choice of \mathbf{J} and \mathbf{A} as in Fig. 2 but lower the size of the system to a 10×10 lattice ($M = 100$ cells) to facilitate computation and visualization. The initial tissue

configuration (Fig. 3A, left) is composed of single-cell types that are stable in isolation (i.e. in the absence of signaling), and it therefore remains stable for very mild levels of cell-cell signaling. However, once γ passes a certain threshold, the tissue is destabilized and self-organizes into a different stable configuration. These multicellular patterns are characterized by signaling-dependent single-cell states (i.e. they are maintained by cell-cell interactions). As γ increases the tissue undergoes a cascade of such transitions which are punctuated by intervals of stability. At $\gamma \gtrsim 1$ the tissue reaches a limiting configuration which no longer changes with increasing signal strength, which we term the strong signaling regime.

Fig. 3A displays only a few of the many tissue transitions which are observed from this particular initial condition. While the transition sequence appears quite complex overall, the earliest transitions at low γ may be anticipated with the following heuristic. By definition, a given tissue state is stable if all cells $\{\mathbf{s}^a\}$ present in the tissue are stable, as defined by Eq. (8). Because the tissue states at $\gamma = 0$ consist of only stable single-cell types ξ^μ , we can readily enumerate the possible neighborhoods (which are defined by the adjacency matrix \mathbf{A}). These neighborhoods determine the collective signaling field experienced by a given cell, Eq. (4). The simplest neighborhood present in the initial condition in Fig. 3A consists of a cell in state ξ^μ surrounded by $z \equiv 8$ cells also in state ξ^μ (z is the coordination number for \mathbf{A}). Recall that the right half of the lattice is composed of ξ^1 while the left half is composed of ξ^2 . We therefore ask: at what γ does the fixed point condition $\xi^\mu = \text{sgn}(\xi^\mu + \gamma z \mathbf{W} \xi^\mu)$ no longer hold? For $\mu = 1$ this criterion gives $\gamma_1^* \approx 0.0231$, whereas for $\mu = 2$ it gives $\gamma_2^* \approx 0.0559$. This analysis is reflected in Fig. 3A, which shows that by $\gamma = 0.024$ the right half is destabilized but not the left, and by $\gamma = 0.056$ the left half

becomes destabilized as well. A general consequence of this analysis is that the encoded single-cell types $\{\xi^\mu\}_{\mu=1}^p$ are destabilized in a sequential fashion, from which we identify at least $\sim p$ low- γ transitions. This heuristic is less useful for describing the many transitions at intermediate levels of γ because it requires enumerating all possible neighborhoods and the combinatorics become prohibitive.

3.3 Nonlinear dimension reduction reveals the emergence of self-organized tissue types

To generalize beyond a single initial condition, we numerically investigate the distribution of stable gene expression states (of the entire tissue) reached by an ensemble of initial conditions. Specifically, we choose $k = 10^4$ random initial conditions $\{\mathbf{x}_i^0\}$ and for each we compute the stable tissue \mathbf{x}_i which self-organizes at a particular value of γ . This mapping generates a large matrix $\mathbf{X}_\gamma \in \{+1, -1\}^{NM \times k}$. Each column of \mathbf{X}_γ , denoted \mathbf{x}_i , is a local minimum of Eq. (5) (equivalently, fixed points of Eq. (8)).

The volume of high-dimensional data makes it challenging to manually identify relationships between local minima \mathbf{x}_i . We therefore use an unsupervised approach to identify points which exhibit similar gene expression patterns. Specifically, we use Uniform Manifold Approximation and Projection (UMAP) (59), a nonlinear dimension reduction technique. Despite the high-dimensionality of this data, UMAP is able to generate an informative two-dimensional embedding. In Fig. 3B we display the nonlinear embedding of \mathbf{X}_γ for several representative values of γ . Each point in a given panel corresponds to a stable tissue \mathbf{x}_i , and we color these points by $n(\mathbf{x}_i)$ which denotes the number of unique single-cell states that are present in the tissue.

At $\gamma = 0$, the points are embedded in a relatively unstructured manner. This is expected and suggests that the

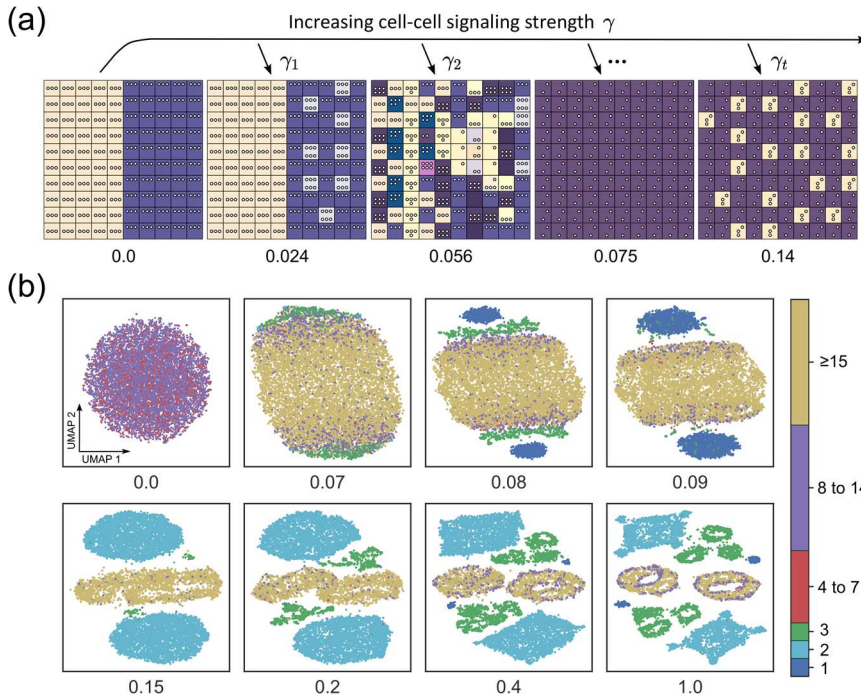


Fig. 3. Emergence of clusters of stable tissue patterns through cell-cell signaling. We fix \mathbf{J} as in Fig. 2 and sample a particular set of cell-cell signaling rules $W_{ij} \sim U[-1,1]$. We use the same type of adjacency matrix \mathbf{A} as in Fig. 2 but with a 10×10 lattice ($M = 100$ cells). (A) From a specific tissue initial condition we increase γ and identify the resulting stable configuration. Numerous tissue transitions are observed as γ is tuned (see Fig. 2 for visualization details). (B) We fix $k = 10^4$ random initial conditions and compute the corresponding stable tissue states $\mathbf{x}_i \in \{+1, -1\}^{NM}$ (N genes, M cells) for eight different values of γ . For each γ , this generates a matrix $\mathbf{X} \in \{+1, -1\}^{NM \times k}$. We embed \mathbf{X} in two dimensions using nonlinear dimension reduction (aligned UMAP (59)). Each point \mathbf{x}_i is colored according to the number of unique single cell states present in the tissue, $n(\mathbf{x}_i)$.

way we are sampling local minima (choice and size of the initial condition ensemble) is not overtly biased. A heuristic argument for this observation is as follows: in the absence of interactions ($\gamma = 0$), a tissue state is stable whenever each cell is stable. The number of stable single-cell states n includes the p encoded single-cell types $\{\xi^\mu\}$ but can also include additional spurious stable states. For the system with $p = 3$ encoded cell types considered in this paper, there are $n = 8$ stable states (Fig. 2B). This gives n^M distinct stable tissue states. When this very large space of n^M minima is sub-sampled at random, one expects little structure in the pairwise distances between sampled minima. This disorder is ultimately reflected in the embedding.

As γ increases this unstructured fine-scale diversity of non-interacting cells in arbitrary spatial arrangements gradually coalesces into a relatively small number of clusters. Interestingly, these clusters have a clear signature in terms of $n(\mathbf{x})$ – the unique single-cell states that are present in the tissue – as well as the energy $\mathcal{H}(\mathbf{x})$ Eq. (5) (see Fig. S2). This indicates that the embedding is clustering distinct “types” of tissue (in analogy to cell types) which maintain some intra-cluster variation. For instance, for $\gamma \geq 0.15$ there are two large clusters which contain tissues comprised of just two cell states. These feature will be explored in more detail in the next section.

Overall, tuning the interaction strength γ promotes the self-organization of the multicellular system into a wide array of stable tissue configurations. At $\gamma = 0$, the model is simply a collection of M non-interacting single-cell types. As γ increases, multicellular structures emerge through collective interactions between the cells. We have shown that the low- γ transitions are associated with sequential destabilization of the encoded single-cell types, whereas the transitions for higher γ are more nuanced. In the next section, we show that the unsupervised approach we take here is especially useful for identifying and distinguishing tissue types in the strong signaling regime.

3.4 Strong signaling causes the tissue to self-organize into a relatively small number of types

In the preceding section, we applied nonlinear dimension reduction to the stable gene expression patterns \mathbf{X}_γ reached from an ensemble of random initial conditions. We showed that the self-organized tissue states form several clusters in the low-dimensional space as γ is increased. Here we focus on \mathbf{X}_γ in the limiting regime of strong signaling ($\gamma = 1$). Fig. 4A shows the UMAP embedding of $\mathbf{X}_{\gamma=1}$ colored by the number of unique single-cell states present in the tissue, $n(\mathbf{x}_i)$. Several representative points from each cluster are annotated and visualized in Fig. 4B.

By comparing the annotated points within and between the clusters, we conclude that this unsupervised approach is producing intuitive clusters which group very similar tissue states (e.g. Fig. 4B, examples 4, 5, 6) while separating very different ones. In analogy to “cell types”, which are defined based on clusters of scRNA-seq data (and specified by gene expression signatures ξ^μ), we refer to these clusters as “tissue

types”. In particular, we observe clusters of maze and strip-like patterns wherein each cell is in one of two specific cell states (Fig. 4B, examples 4-6, 11, 12), clusters where the tissue gene expression is homogeneous (Fig. 4B, examples 1 and 9), and clusters which consist of tissue types that each are composed of two of the aforementioned tissue types separated by an interface (Fig. 4B, examples 2, 7, 8, 10).

We also note that within each cluster described above, there can be extensive fine-scale variation (for instance, in the spatial arrangement of cell states within the maze-like clusters). This suggests a hierarchical picture of the multicellular energy landscape Eq. (5). At a high level, the landscape is partitioned into several basins of attraction corresponding to the different tissue types. In more detail, each of these basins may be locally very rugged (i.e. contain many local minima in close proximity), reflecting the large number of similar but distinct stable tissue configurations we observe in some of the clusters.

Additionally, we observe that these clusters appear in symmetric pairs. Inspection of the elements of each pair reveals that they have opposite gene expression patterns (i.e. $\{\mathbf{s}^a\} \rightarrow \{-\mathbf{s}^a\}$, compare e.g. Fig. 4B points 6 and 12). This is a reflection of the spin-flip symmetry present in Eq. (5), and indicates that the way the local minima are being sampled (i.e. the ensemble size and dynamical update rule) is sufficient to capture expected aspects of the energy landscape in a relatively unbiased manner. As an aside, the antisymmetric minima can be eliminated by applying an external field to the gene expression of each cell (e.g. by biasing certain “housekeeping” genes to remain on), and this will be investigated in further work.

Separately, we also report the distribution of both $n(\mathbf{x}_i)$ and the multicellular energy $E = \mathcal{H}(\mathbf{x}_i)$ over all sampled minima $\{\mathbf{x}_i\}_{i=1}^k$ of $\mathcal{H}(\mathbf{x})$. We display the data in Fig. 4C, which contains a scatter plot as well as the two marginal distributions (i.e. $p(n)$ and $p(E)$). In Fig. 4D we provide a version of Fig. 4A colored instead by $E = \mathcal{H}(\mathbf{x}_i)$.

The data exhibits three main features. First, there is a clear correlation between $n(\mathbf{x}_i)$ and $\mathcal{H}(\mathbf{x}_i)$ (note this is also apparent when comparing Fig. 4A and D). This means that the deepest minima tend to be highly ordered states characterized by a low number of unique single-cell states (low n – as exemplified, for instance, by point 1 in Fig. 4B). In contrast, the higher energy minima tend to be more disordered with large numbers of distinct single-cell states n , illustrated by point 3 in Fig. 4B. Second, these low energy, highly ordered minima are also the most probable (over an ensemble of random initial conditions). This is reflected in the small n , low energy peaks in $p(n)$ and $p(E)$. In terms of the energy landscape, this suggests that the basins of attraction for these deep ordered states have large volume. And third, looking specifically at the distribution of the number of single-cell states within a tissue, $p(n)$, there is a smooth “bulk” of disordered minima with $5 < n < 35$ which appears bimodal.

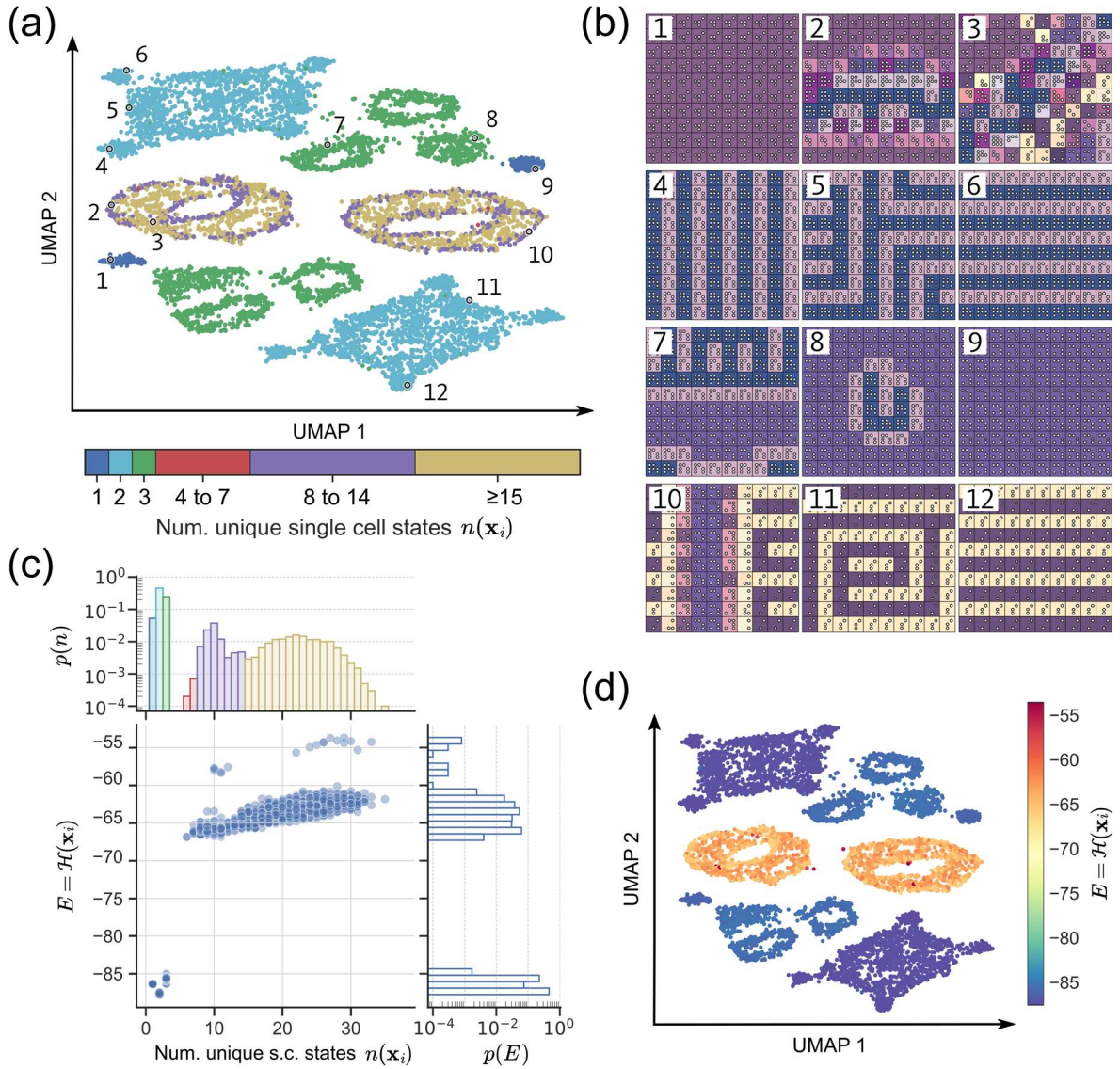


Fig. 4. Distribution of stable tissue configurations for strong signaling. (A) The $\gamma = 1$ sub-panel of Fig. 3B is shown with (B) twelve representative examples from the observed clusters (see Fig. 2 for visualization details). (C) For each point \mathbf{x}_i from panel A, the number of unique single cell states present in the tissue, $n(\mathbf{x}_i)$, is plotted against the energy $E = \mathcal{H}(\mathbf{x}_i)$ (Eq. (5)). Histograms are shown for both distributions. (D) The embedding from panel A is colored according to the multicell Hamiltonian $\mathcal{H}(\mathbf{x}_i)$.

In the following section we investigate how these properties of the local minima of Eq. (5) depend on the choice of random cell-cell signaling rules \mathbf{W} .

3.5 Distribution of stable tissues under different random signaling rules displays universal characteristics

In the strong signaling regime we observe several striking features of the distribution of stable tissue configurations ($\gamma = 1$ data shown in Fig. 4). Here we investigate to what extent these features are preserved under different realizations of the random cell-cell signaling rules \mathbf{W} .

As above we denote the frequency of local minima with n unique single-cell states by $p(n)$, and the frequency of local

minima with energy $E = \mathcal{H}(\mathbf{x})$ by $p(E)$. For eight different signaling rules $\{\mathbf{W}_\alpha\}_{\alpha=1}^8$, we sample the local minima (self-organized tissue configurations) reached by an ensemble of random initial conditions of the tissue gene expression. The signaling rules \mathbf{W}_α have uniformly distributed elements between -1 and 1 , $W_{ij} \sim U[-1, 1]$. The data for each \mathbf{W}_α is shown in the Fig. 5. Each panel shows a scatter plot of $n(\mathbf{x}_i), \mathcal{H}(\mathbf{x}_i)$ for the sampled minima $\{\mathbf{x}_i\}$ as well as the marginal distributions $p(n), p(E)$.

Despite some expected variation between the eight plots, the three features identified in the preceding section are largely preserved. All plots exhibit a positive correlation between the energy E and the number of unique single-cell

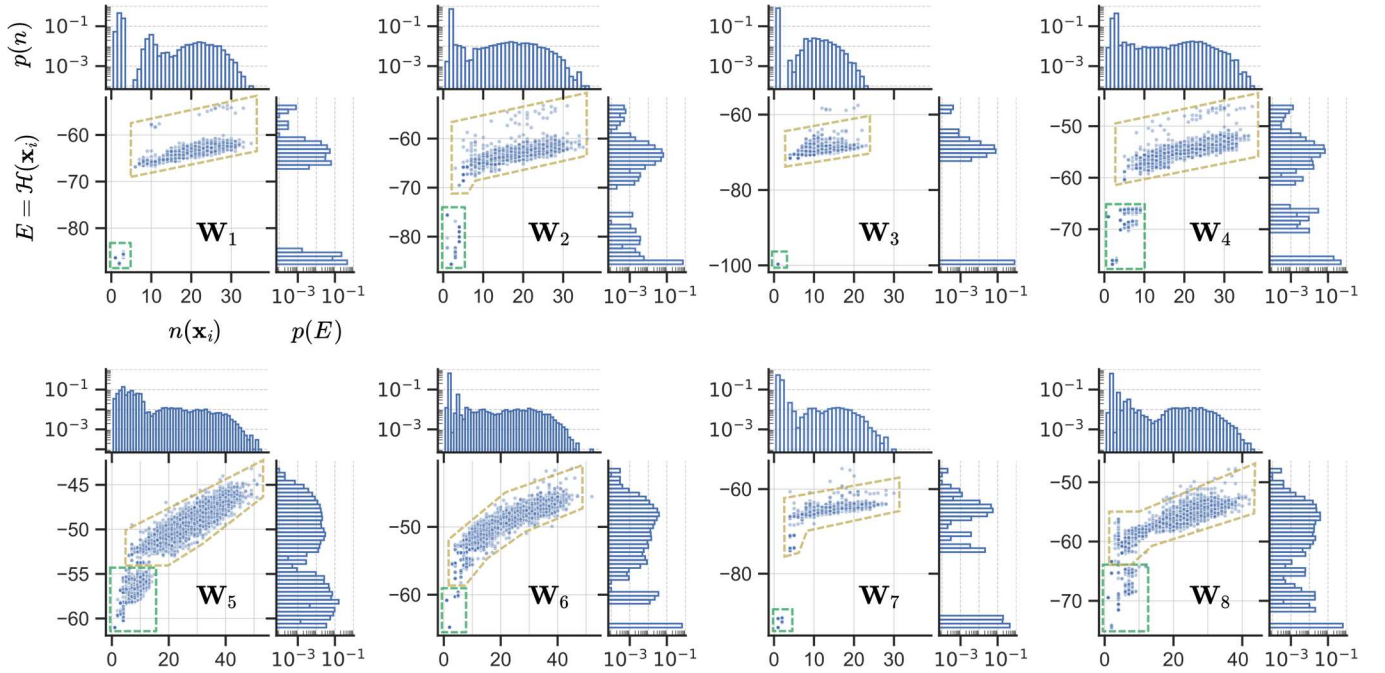


Fig. 5. Distribution of stable tissues under different signaling rules. Eight signaling matrices $\{\mathbf{W}_\alpha\}$ are sampled according to $W_{ij} \sim U[-1, 1]$. For each \mathbf{W}_α , the space of stable tissues (local minima of Eq. (5)) is sampled via $k = 10^4$ random initial conditions at $\gamma = 1$. For each stable tissue \mathbf{x}_i , we compute its energy $E = \mathcal{H}(\mathbf{x}_i)$ and the number of unique single cell states $n(\mathbf{x}_i)$. Each panel visualizes the joint distribution of these quantities as well as their marginal distributions $p(n)$, $p(E)$. The dashed green (gold) box denotes the ordered, low energy (disordered, high energy) segments of the distribution. The top-left panel \mathbf{W}_1 corresponds to the cell-cell signaling rules used in Figs. 3 and 4. All panels use the same \mathbf{J} , \mathbf{A} as in Figs. 3 and 4.

states n . This indicates that the deepest minima in the energy landscape Eq. (5) are also the simplest (i.e. composed of few types of cells), which is denoted in Fig. 5 by the dashed green box. Likewise, the more disordered minima (large n) tend to have higher energies and also form a “bulk” (indicated by a dashed gold box in Fig. 5) which also has a positive slope. In all plots we see that these ordered, deep minima appear with much higher probability (note the logarithmic scale) than the disordered, shallow minima.

This data suggests that, in the strong interaction regime, the energy landscape exhibits several universal features which are relatively invariant under different realizations of the cell-cell interaction matrix \mathbf{W} . Minor deviations arising from atypical \mathbf{W} are observed, (e.g. the lack of a strong single peak at low n for \mathbf{W}_5). Most notably, the lowest energy minima tend to also be the most ordered minima, as quantified by $n(\mathbf{x})$. Furthermore, these deep, ordered minima appear to have large basins of attraction when compared to the “bulk” of more disordered, shallow minima.

4. SUMMARY AND DISCUSSION

We have presented a model of multicellular gene expression which couples single cell gene-regulation with cell-cell signaling in a tunable manner. This tunability allows us to systematically study how initially non-interacting single cells can self-organize into a variety of stable tissue types as the cell-cell signaling strength γ is tuned.

Specifically, we have investigated the distribution of stable tissues represented by the local minima of the tissue gene expression landscape at various levels of signaling strength γ . In the strong signaling regime, we identify several semi-universal properties which appear to be preserved across different realizations of the random cell-cell signaling rules. These results may point to organizing principles for multicellular organisms and other complex systems with modular structure, such as self-assembling materials and social networks.

The basic unit of the model, the single cell, is parameterized solely by a set of gene expression vectors $\{\xi^\mu\}$ corresponding to prescribed single-cell types. These cell types are encoded as stable fixed points of a Hopfield network (HN), defining a gene-gene interaction matrix \mathbf{J} . At the multicellular level, all cells have the same internal rules \mathbf{J} , and interact according to a spatial adjacency matrix \mathbf{A} and a cell-cell signaling matrix $\gamma\mathbf{W}$ which couples the gene expression of adjacent cells. For the disordered cell-cell interactions we consider here, the resulting model of tissue is a type of spin glass with a repeating block structure (Fig. 1C).

This model of multicellular gene expression displays striking self-organizing properties. When the multicell lattice is initialized with simple spatial patterns of single cells (such as one cell type on the left half of the lattice, and another cell type on the right half), it morphs into a stable configuration determined by the interplay of intracellular gene regulation \mathbf{J}

and the cell-cell signaling rules \mathbf{W} . Notably, stable configurations of the multicell collective can include single-cell states which are unstable in the absence of signaling. This may be important in different biological contexts where the strength of collective signaling varies, such as wound healing and the immune response. A diverse range of stable tissue configurations is observed when we sample different \mathbf{W} (Fig. 2), including homogeneous patterns, “spotted” patterns, maze-like structures, and multiphase configurations with distinct patterns that are separated by an interface. The spatial features of the observed patterns also scale with the cell-cell interaction distance. It will be important to investigate in future work if, given \mathbf{J} , \mathbf{W} , \mathbf{A} , and γ , one can predict the types of tissues which may self-organize. For instance, what are the characteristics of the model parameters which enable maze-like patterns?

The cell-cell signaling strength γ tunes the strength of the intercellular interactions $\gamma\mathbf{W}$ relative to the intracellular interactions \mathbf{J} . When both sets of gene regulatory rules (\mathbf{J} , \mathbf{W}) are held fixed, and only γ is tuned, the model displays rich behavior, including numerous transitions in the structure of the space of stable tissues. At $\gamma = 0$ the multicell model describes M non-interacting replicas of the single model. Beyond a certain critical value $\gamma > \gamma_c$ collective multicellular behavior emerges, characterized by self-organizing tissue states which are unstable in the absence of signaling. We have identified $\sim p$ low- γ transitions corresponding to sequential destabilization of the encoded cell types. The subsequent tissue transitions at higher γ depend on the detailed structure of \mathbf{J} and \mathbf{W} , and will be investigated in future work.

Our analysis of the strong signaling regime suggests that the distribution of stable tissue configurations can be grouped into a relatively small number of classes which we refer to as tissue types. This gives a hierarchical picture of the energy landscape of tissue gene expression. The state space is partitioned into several large basins of attraction which correspond to the identified tissue types. Within these macroscopic attractors there can be many subtly distinct minima, such that these tissue type basins can be very rugged locally. We refer to this phenomenon as “fine-scale diversity” of a given tissue type. Interestingly, our results suggest that several features of the energy landscape are invariant to different realizations of the random cell-cell signaling rules. In particular, we found that minima depth and simplicity (as characterized by number of unique single-cell states and spatial structure) were positively correlated. Additionally, these deep, simple minima tend to have very large basins of attraction compared to the less ordered, shallow minima. These results may explain why multicellular tissues in different organisms robustly self-organize into relatively simple configurations (composed of few unique cell states) despite the microscopic interactions which drive the system – defined here by the cell-cell signaling networks – being highly disordered. These observations may have implications in other contexts, such as hierarchical self-organization in neuroscience (60, 61) and

in non-biological systems including material self-assembly (62).

In natural systems, escape from a particular tissue type may represent a breakdown of tissue homeostasis and the initiation of a chronic disease process. Such transitions can arise from stochasticity in gene expression, or can be driven by extrinsic factors such as environmental changes including drugs or direct changes to tissue composition such as wounding – which can be represented in the model as external applied fields. Each of these plays an important role in disease initiation and progression, and will be considered in future analyses of the framework developed in this paper. The analysis of transitions between stable multicell states in our framework may be particularly relevant for understanding major diseases associated with aging, most notably chronic autoimmunity and cancer, which are characterized by stable changes in the phenotypic composition of tissue.

Our work has implications for how “cell type” should be defined (63). Modern experimental techniques which can measure gene expression in millions of single cells at a time allow us to observe cell state in unprecedented detail. This has led to significant international effort (16, 18) to catalog the cell types found in human tissue, with the ultimate goal of understanding and treating disease. A common approach to define cell type is based on the identification of clusters of similar cells in single-cell gene expression data. In our framework, the fixed points of the multicellular system clearly change as the strength of signaling γ changes. Varying cell-cell interaction strength may be an important consideration when analyzing natural systems, especially during the experimental data collection. At low γ the prescribed single-cell types are by definition stable, but at high γ they can be destabilized as multicellular structures emerge. *In vivo*, cells are continuously interacting and these interactions affect which cell states are stable or unstable. Modern definitions of biological cell type must be made to accommodate this.

An important next step for the framework presented here is to incorporate cellular birth and death. This will enable deeper connections to broader biological processes, of which multicellular development is perhaps the most fascinating and ubiquitous. During mammalian development the multicell system robustly “unfolds” from a single cell in a particular embryonic state to, eventually, an adult organism comprised of trillions of cells. Despite the complexity and duration of the process, it occurs with remarkable predictability. Introducing cellular division to our framework will lead to a cascade of self-organized transitions of the multicell system reminiscent of the developmental unfolding process (64). The intra- and intercellular regulatory rules \mathbf{J} , \mathbf{W} will determine the fate of these unfolding trajectories.

Acknowledgements

We acknowledge the support of the Natural Sciences and Engineering Research Council of Canada (NSERC) through Discovery Grant RGPIN 402591 to A.Z. and CGS-D

Graduate Fellowship to M.S. We thank Duncan Kirby and Jeremy Rothschild for helpful discussions.

References

1. K. Takahashi, S. Yamanaka, Induction of Pluripotent Stem Cells from Mouse Embryonic and Adult Fibroblast Cultures by Defined Factors. *Cell* **126**, 663–676 (2006).
2. J. Xu, Y. Du, H. Deng, Direct lineage reprogramming: Strategies, mechanisms, and applications. *Cell Stem Cell* **16**, 119–134 (2015).
3. M. V. Plikus, *et al.*, Regeneration of fat cells from myofibroblasts during wound healing. *Science (80-.)*. **355**, 748–752 (2017).
4. M. Sinha, *et al.*, Direct conversion of injury-site myeloid cells to fibroblast-like cells of granulation tissue. *Nat. Commun.* **9**, 1–19 (2018).
5. C. F. Guerrero-Juarez, *et al.*, Single-cell analysis reveals fibroblast heterogeneity and myeloid-derived adipocyte progenitors in murine skin wounds. *Nat. Commun.* **10** (2019).
6. F. de Sousa e Melo, F. J. de Sauvage, Cellular Plasticity in Intestinal Homeostasis and Disease. *Cell Stem Cell* **24**, 54–64 (2019).
7. S. Yuan, R. J. Norgard, B. Z. Stanger, Cellular plasticity in cancer. *Cancer Discov.* **9**, 837–851 (2019).
8. A. L. Means, *et al.*, Pancreatic epithelial plasticity mediated by acinar cell transdifferentiation and generation of nestin-positive intermediates. *Development* **132**, 3767–3776 (2005).
9. M. Smart, S. Goyal, A. Zilman, Roles of phenotypic heterogeneity and microenvironment feedback in early tumor development. *Phys. Rev. E* **103**, 032407 (2021).
10. V. Giroux, A. K. Rustgi, Metaplasia: Tissue injury adaptation and a precursor to the dysplasia-cancer sequence. *Nat. Rev. Cancer* **17**, 594–604 (2017).
11. C. H. Waddington, *The strategy of the genes. A discussion of some aspects of theoretical biology.* (London: Allen & Unwin, 1957).
12. S. Huang, G. Eichler, Y. Bar-Yam, D. E. Ingber, Cell fates as high-dimensional attractor states of a complex gene regulatory network. *Phys. Rev. Lett.* **94**, 1–4 (2005).
13. H. H. Chang, M. Hemberg, M. Barahona, D. E. Ingber, S. Huang, Transcriptome-wide noise controls lineage choice in mammalian progenitor cells. *Nature* **453**, 544–547 (2008).
14. S. Huang, The molecular and mathematical basis of Waddington’s epigenetic landscape: A framework for post-Darwinian biology? *BioEssays* **34**, 149–157 (2012).
15. J. Wang, K. Zhang, L. Xu, E. Wang, Quantifying the Waddington landscape and biological paths for development and differentiation. *Proc. Natl. Acad. Sci.* **108**, 8257–8262 (2011).
16. A. Regev, *et al.*, Science Forum: The Human Cell Atlas. *Elife*, 1–30 (2017).
17. X. Han, *et al.*, Mapping the Mouse Cell Atlas by Microwell-Seq. *Cell* **172**, 1091–1107.e17 (2018).
18. M. Karlsson, *et al.*, A single-cell type transcriptomics map of human tissues. *Sci. Adv.* **7** (2021).
19. A. M. Turing, The chemical basis of morphogenesis. *Philos. Trans. R. Soc. Lond. B. Biol. Sci.* **237**, 37–72 (1952).
20. T. Maire, H. Youk, Molecular-Level Tuning of Cellular Autonomy Controls the Collective Behaviors of Cell Populations. *Cell Syst.* **1**, 349–360 (2015).
21. E. P. Olimpio, Y. Dang, H. Youk, Statistical Dynamics of Spatial-Order Formation by Communicating Cells. *iScience* **2**, 27–40 (2018).
22. Y. Dang, D. A. J. Grundel, H. Youk, Cellular Dialogues: Cell-Cell Communication through Diffusible Molecules Yields Dynamic Spatial Patterns. *Cell Syst.* **10**, 82–98.e7 (2020).
23. J. M. Osborne, A. G. Fletcher, J. M. Pitt-Francis, P. K. Maini, D. J. Gavaghan, Comparing individual-based approaches to modelling the self-organization of multicellular tissues. *PLoS Comput. Biol.* **13** (2017).
24. S. Jang, *et al.*, Dynamics of embryonic stem cell differentiation inferred from single-cell transcriptomics show a series of transitions through discrete cell states. *Elife* **6** (2017).
25. J. Kim, B. K. Koo, J. A. Knoblich, Human organoids: model systems for human biology and medicine. *Nat. Rev. Mol. Cell Biol.* **21**, 571–584 (2020).
26. M. M. Babu, N. M. Luscombe, L. Aravind, M. Gerstein, S. A. Teichmann, Structure and evolution of transcriptional regulatory networks. *Curr. Opin. Struct. Biol.* **14**, 283–291 (2004).
27. J. J. Hopfield, Neural networks and physical systems with emergent collective computational abilities. *Proc. Natl. Acad. Sci. U. S. A.* **79**, 2554–2558 (1982).
28. D. J. Amit, *Modeling Brain Function: The World of Attractor Neural Networks* (Cambridge University Press, 1989) <https://doi.org/10.1017/cbo9780511623257>.
29. A. H. Lang, H. Li, J. J. Collins, P. Mehta, Epigenetic Landscapes Explain Partially Reprogrammed Cells and Identify Key Reprogramming Genes. *PLoS Comput. Biol.* **10** (2014).
30. S. T. Pusuluri, A. H. Lang, P. Mehta, H. E. Castillo, Cellular reprogramming dynamics follow a simple 1D reaction coordinate. *Phys. Biol.* **15** (2018).
31. S. A. Kauffman, Metabolic stability and epigenesis in randomly constructed genetic nets. *J. Theor. Biol.* **22**, 437–467 (1969).
32. M. Mojtahedi, *et al.*, Cell Fate Decision as High-Dimensional Critical State Transition. *PLoS Biol.* **14**

- (2016).
33. D. J. Amit, H. Gutfreund, H. Sompolinsky, Spin-glass models of neural networks. *Phys. Rev. A* **32**, 1007–1018 (1985).
 34. I. Kanter, H. Sompolinsky, Associative recall of memory without errors. *Phys. Rev. A* **35**, 380–392 (1987).
 35. L. Personnaz, I. Guyon, G. Dreyfus, Collective computational properties of neural networks: New learning mechanisms. *Phys. Rev. A* **34**, 4217–4228 (1986).
 36. A. Szedlak, S. Sims, N. Smith, G. Paternostro, C. Piermarocchi, Cell cycle time series gene expression data encoded as cyclic attractors in Hopfield systems. *PLoS Comput. Biol.* **13**, 1–19 (2017).
 37. A. T. Fard, M. A. Ragan, Modeling the attractor landscape of disease progression: A network-based approach. *Front. Genet.* **8**, 1–11 (2017).
 38. A. T. Fard, S. Srihari, J. C. Mar, M. A. Ragan, Not just a colourful metaphor: Modelling the landscape of cellular development using hopfield networks. *npj Syst. Biol. Appl.* **2** (2016).
 39. J. Guo, J. Zheng, HopLand: Single-cell pseudotime recovery using continuous Hopfield network-based modeling of Waddington’s epigenetic landscape in *Bioinformatics*, (2017), pp. i102–i109.
 40. S. R. Maeschke, M. A. Ragan, Characterizing cancer subtypes as attractors of Hopfield networks. *Bioinformatics* **30**, 1273–1279 (2014).
 41. H. Knöpfel, M. Löwe, K. Schubert, A. Sinulis, Fluctuation Results for General Block Spin Ising Models. *J. Stat. Phys.* **178**, 1175–1200 (2020).
 42. W. Kirsch, G. Toth, Two Groups in a Curie–Weiss Model with Heterogeneous Coupling. *J. Theor. Probab.* **33**, 2001–2026 (2020).
 43. M. Fedele, P. Contucci, Scaling Limits for Multi-species Statistical Mechanics Mean-Field Models. *J. Stat. Phys.* **144**, 1186–1205 (2011).
 44. A. Barra, G. Genovese, F. Guerra, Equilibrium statistical mechanics of bipartite spin systems. *J. Phys. A Math. Theor.* **44**, 1–23 (2011).
 45. A. Barra, P. Contucci, E. Mingione, D. Tantari, Multi-Species Mean Field Spin Glasses. Rigorous Results. *Ann. Henri Poincaré* **16**, 691–708 (2015).
 46. D. Panchenko, The free energy in a multi-species Sherrington-Kirkpatrick model. *Ann. Probab.* **43**, 3494–3513 (2015).
 47. E. Agliari, D. Migliozi, D. Tantari, Non-convex Multi-species Hopfield Models. *J. Stat. Phys.* **172**, 1247–1269 (2018).
 48. K. Kaneko, Overview of coupled map lattices. *Chaos* **2**, 279–282 (1992).
 49. R. R. Klevecz, Phenotypic heterogeneity and genotypic instability in coupled cellular arrays. *Phys. D Nonlinear Phenom.* **124**, 1–10 (1998).
 50. F. A. Bignone, Cells-gene interactions simulation on a coupled map lattice. *J. Theor. Biol.* **161**, 231–249 (1993).
 51. V. García-Morales, J. A. Manzanares, S. Mafe, Weakly coupled map lattice models for multicellular patterning and collective normalization of abnormal single-cell states. *Phys. Rev. E* **95**, 1–24 (2017).
 52. R. J. Glauber, Time-dependent statistics of the Ising model. *J. Math. Phys.* **4**, 294–307 (1963).
 53. J. J. Hopfield, Neurons with graded response have collective computational properties like those of two-state neurons. *Proc. Natl. Acad. Sci. U. S. A.* **81**, 3088–3092 (1984).
 54. K. ichi Funahashi, Y. Nakamura, Approximation of dynamical systems by continuous time recurrent neural networks. *Neural Networks* **6**, 801–806 (1993).
 55. M. Aguilera, S. A. Moosavi, H. Shimazaki, A unifying framework for mean-field theories of asymmetric kinetic Ising systems. *Nat. Commun.* **12** (2021).
 56. Y. Roudi, E. Aurell, J. A. Hertz, Statistical physics of pairwise probability models. *Front. Comput. Neurosci.* **3** (2009).
 57. M. Mézard, J. Sakellariou, Exact mean-field inference in asymmetric kinetic Ising systems. *J. Stat. Mech. Theory Exp.* **2011** (2011).
 58. A. Lo Cicero, P. D. Stahl, G. Raposo, Extracellular vesicles shuffling intercellular messages: For good or for bad. *Curr. Opin. Cell Biol.* **35**, 69–77 (2015).
 59. L. McInnes, J. Healy, J. Melville, UMAP: Uniform Manifold Approximation and Projection for Dimension Reduction. *arXiv:1802.03426v3* (2018).
 60. D. O’Kane, A. Treves, Short- and long-range connections in autoassociative memory. *J. Phys. A. Math. Gen.* **25**, 5055–5069 (1992).
 61. M. Naim, V. Boboeva, C. J. Kang, A. Treves, Reducing a cortical network to a Potts model yields storage capacity estimates. *J. Stat. Mech. Theory Exp.* **2018** (2018).
 62. A. Murugan, Z. Zeravcic, M. P. Brenner, S. Leibler, Multifarious assembly mixtures: Systems allowing retrieval of diverse stored structures. *Proc. Natl. Acad. Sci. U. S. A.* **112**, 54–59 (2015).
 63. , What Is Your Conceptual Definition of “Cell Type” in the Context of a Mature Organism? *Cell Syst.* **4**, 255–259 (2017).
 64. A. Stanoev, C. Schröter, A. Koseska, Robustness and timing of cellular differentiation through population-based symmetry breaking. *Dev.* **148** (2021).

Supplementary Information for “Emergent properties of collective gene expression patterns in multicellular systems”
 Matthew Smart and Anton Zilman

Numerical methods and software: Python 3.8 is used for all simulations, data analyses, and visualizations. The following Python libraries were used: NumPy (v1.20.0), SciPy (v1.6.0), Matplotlib (v3.3.4), Scikit-Learn (v0.24.1), ProPlot (v0.6.4), Seaborn (v0.11.1), and UMAP-Learn (v0.5.0).

Embedding of the single cell energy landscape: The single cell energy landscape depicted in Fig. 2B in the main text is produced by computing the Hamming distance between four minima of $\mathcal{H}_0(\mathbf{s})$: ξ^1, ξ^2, ξ^3 and $\mathbf{S} = \frac{1}{3}(\xi^1 + \xi^2 + \xi^3)$, and each of the 2^N gene expression states $\{\mathbf{s}\}$. This results in a matrix $\mathbf{X} \in \mathbb{R}^4 \times 2^N$. Principle component analysis (PCA) is then applied to \mathbf{X} to obtain a two-dimensional embedding $\tilde{\mathbf{X}} \in \mathbb{R}^2 \times 2^N$. The columns of $\tilde{\mathbf{X}}$ correspond to embeddings of each gene expression state \mathbf{s} , which we plot in three dimensions using $\mathcal{H}_0(\mathbf{s})$ as the vertical axis.

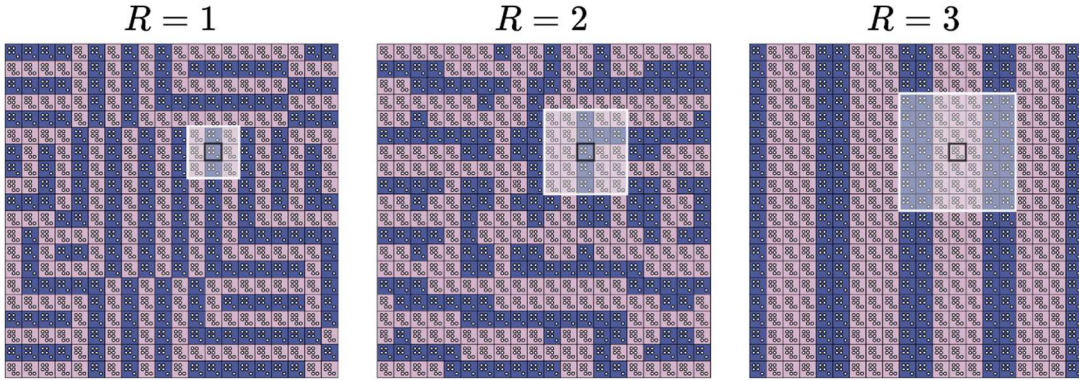


Fig. S1. Tissue patterns scale with signal radius. We choose the “maze-generating” cell-cell signaling rules \mathbf{W} which stabilized the upper left tissue state in Fig. 2D. Details of the visualization approach are provided in Fig. 2. Each tissue is generated from the same dual initial condition as in Fig. 2C for $\gamma = 1$. The interaction radius R , which defines a corresponding adjacency matrix \mathbf{A}_R , is indicated above each tissue. The white shaded region denotes the neighborhood which experiences signaling from the indicated cell.

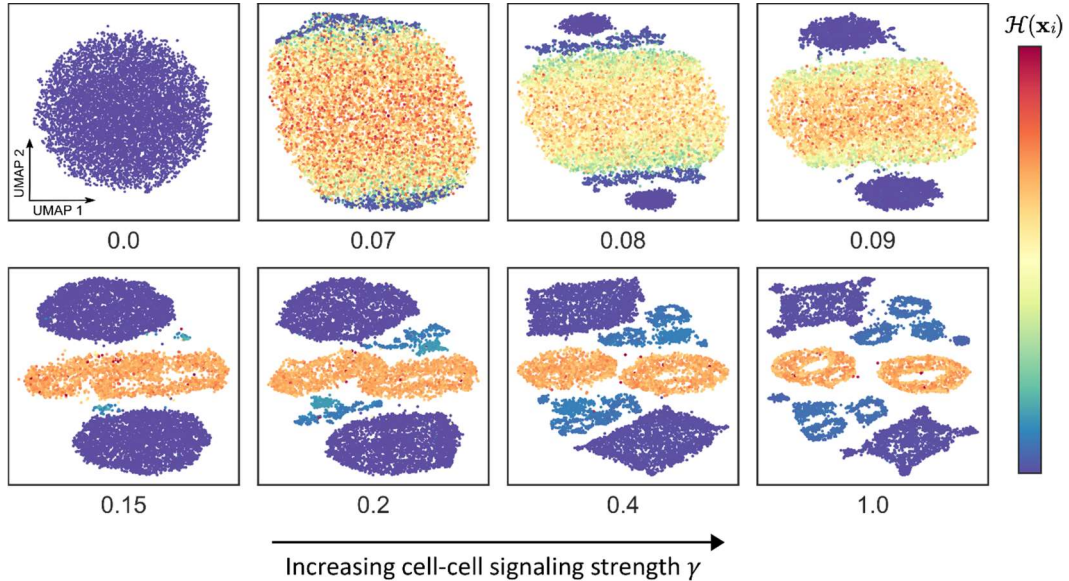


Fig. S2. Relative energy of self-organized tissue states for increasing cell-cell signaling strength γ . Within a panel, each point represents a stable state \mathbf{x}_i of the multicellular gene expression. Here we color each point according to its multicellular energy $\mathcal{H}(\mathbf{x}_i)$. The same sequence of embeddings is visualized in Fig. 3B by $\mathbf{n}(\mathbf{x}_i)$, which counts the number of unique single cell states present in \mathbf{x}_i .

Table S1. Details of each variable and expression in the mathematical model.

Expression	Dimension	Description	Biological Interpretation
N	--	Positive integer.	Number of distinct genes which a single cell may express.
p	--	Positive integer.	Number of stable single cell types. E.g., fibroblast, hepatocyte, etc.
M	--	Positive integer.	Number of cells in the tissue.
\mathbf{s}	N	Generic state vector. Elements $s_i \in \{+1, -1\}$.	Single cell gene expression state (each gene is “on” or “off”).
ξ^μ	N	Special state vectors (“cell types”) indexed by $\mu \in \{1, \dots, p\}$.	Transcriptome of cell type μ .
$\xi = [\xi^1 \xi^2 \dots \xi^p]$	$N \times p$	Cell types arranged as matrix columns.	Transcriptomes of p cell types.
$\mathbf{J} = \xi(\xi^T \xi)^{-1} \xi^T$	$N \times N$	Hopfield network interaction matrix. Elements J_{ij} .	Specifies gene-gene interactions which stabilize the p cell types represented by ξ .
$\mathcal{H}_0(\mathbf{s}) = -\frac{1}{2} \mathbf{s}^T \mathbf{J} \mathbf{s} - \mathbf{h}^T \mathbf{s}$	--	Hamiltonian of an Ising spin glass in an external field \mathbf{h} .	Single cell epigenetic landscape.
$\{\mathbf{s}^a\}_{a=1}^M$	N (each)	Set of M interacting cells (each is N -dimensional).	The gene expression vectors of all cells present in the tissue.
\mathbf{x}	NM	Tissue state represented as a column vector (M cells concatenated).	A gene expression vector describing tissue gene expression.
\mathbf{A}	$M \times M$	Adjacency matrix representing a multicell graph. Elements $A^{ab} \in \{0, 1\}$.	Specifies which cells are interacting (e.g., paracrine signaling).
\mathbf{W}	$N \times N$	Symmetric matrix. Elements randomly sampled as $W_{ij} \sim U[-1, 1]$.	Cell-cell signaling matrix for adjacent cells W_{ij} specifies the effect gene i in cell a has on gene j in cell b .
γ	--	Scales the elements of \mathbf{W} .	Cell-cell signaling strength.
$\mathbf{h}^a = \gamma \sum_b A^{ab} \mathbf{W} \mathbf{s}^b$	N	Applied field cell a receives from its adjacent cells.	Gene expression bias on cell a due to collective cell-cell signaling.
$\mathcal{H}(\{\mathbf{s}^a\}) = -\frac{1}{2} \sum_a \mathbf{s}^{aT} \mathbf{J} \mathbf{s}^a - \frac{\gamma}{2} \sum_a \sum_b A^{ab} \mathbf{s}^{aT} \mathbf{W} \mathbf{s}^b$	--	Block Ising spin glass. The first set of terms accounts for M non-interacting cells. The second set of terms accounts for cell-cell interactions between adjacent cells.	Gene expression landscape for the tissue (set of interacting cells).
$\mathcal{J}(\gamma) = \mathbf{I}_M \otimes \mathbf{J} + \mathbf{A} \otimes \gamma \mathbf{W}$	$NM \times NM$	Multicell interaction matrix in block form. Diagonal blocks are copies of the single cell interactions \mathbf{J} , and off-diagonal blocks are copies of $\gamma \mathbf{W}$ or $\mathbf{0}$.	Interaction matrix for all genes present in the tissue (N genes times M cells).